Proceedings of Meetings on Acoustics

164th Meeting of the Acoustical Society of America
Kansas City, Missouri
22 - 26 October 2012
Session 3aNS: Noise

3aNS9.   Spectral and statistical analysis of noise from reusable solid rocket motors

Kent L. Gee*, R. Jeremy Kenny, Tracianne B. Neilsen, Trevor W. Jerome, Christopher M. Hobbs and Michael M. James

*Corresponding author's address: Physics and Astronomy, Brigham Young University, N283, Provo, UT 84602, kentgee@byu.edu

  As part of investigations into the design of next-generation launch vehicles, near and far-field data were collected during horizontal static firings of reusable solid rocket motors. In addition to spectral analysis at individual microphone locations, the spatial and temporal variation of overall and one-third octave band pressure levels at sideline and polar arc arrays is considered. Analysis of the probability density functions reveals positively skewed pressure waveforms, but extreme skewness in the first-order estimate of the time derivative because of the presence of significant acoustic shocks. However, plume impingement is the likely cause of reduced high-frequency levels and skewness at far-downstream positions.

Published by the Acoustical Society of America through the American Institute of Physics

1. Introduction

For the past several years, the National Aeronautics and Space Administration (NASA) has been designing a crew launch vehicle that has the capability of going beyond lower-Earth orbit, which is the focus of current commercial space-flight ventures. What began with the design for the Ares V vehicle has evolved into the Space Launch System (SLS), of which an artist's depiction is shown in Figure 1. Thrust at SLS launch will be provided by two five-segment reusable solid rocket motors (RSRM) and five Space Shuttle main engines. Determination of how the vibroacoustic loading at launch will impact vehicle and payload design is an important, but challenging, undertaking.

The model currently used for determining the acoustic loading[1] uses empirical curves based on experiments on sub-scale motors and findings from unheated jets. To more appropriately extend the model's capability to these larger motors, NASA funded the measurement of the acoustics around three static four-segment Shuttle RSRM firings at ATK Space Systems in Promontory, UT.[2] Although the data are already being incorporated into modeling efforts,[3, 4, 5, 6] the spatial and temporal features of the spectra and statistics from these tests are the focus of this paper.

Figure 1. Artist rendering of the proposed SLS vehicle. Note the two five-segment solid rocket boosters.

2. Measurement Summary

The three motor tests were designated Technical Evaluation Motor (TEM) -13, Flight Verification Motor (FVM) -2, and Flight Support Motor (FSM) -15. The RSRM motors are fired horizontally toward a hillside at ATK, which can be seen topographically, along with microphone locations in Figure 2. The plume boundary, including nozzle vectoring, is also shown. Thrust profiles and vectoring schedules from the three tests were shown previously in Ref. 2. A simplified schematic of this layout, which correlates directly to the manner in which the results are displayed in this paper, is shown in Figure 3. The nozzle exit diameter is

approximately D = 3.87 m. Data were collected using Type 1 6.35 mm pressure microphones at sampling rates of 48 and 96 kHz.
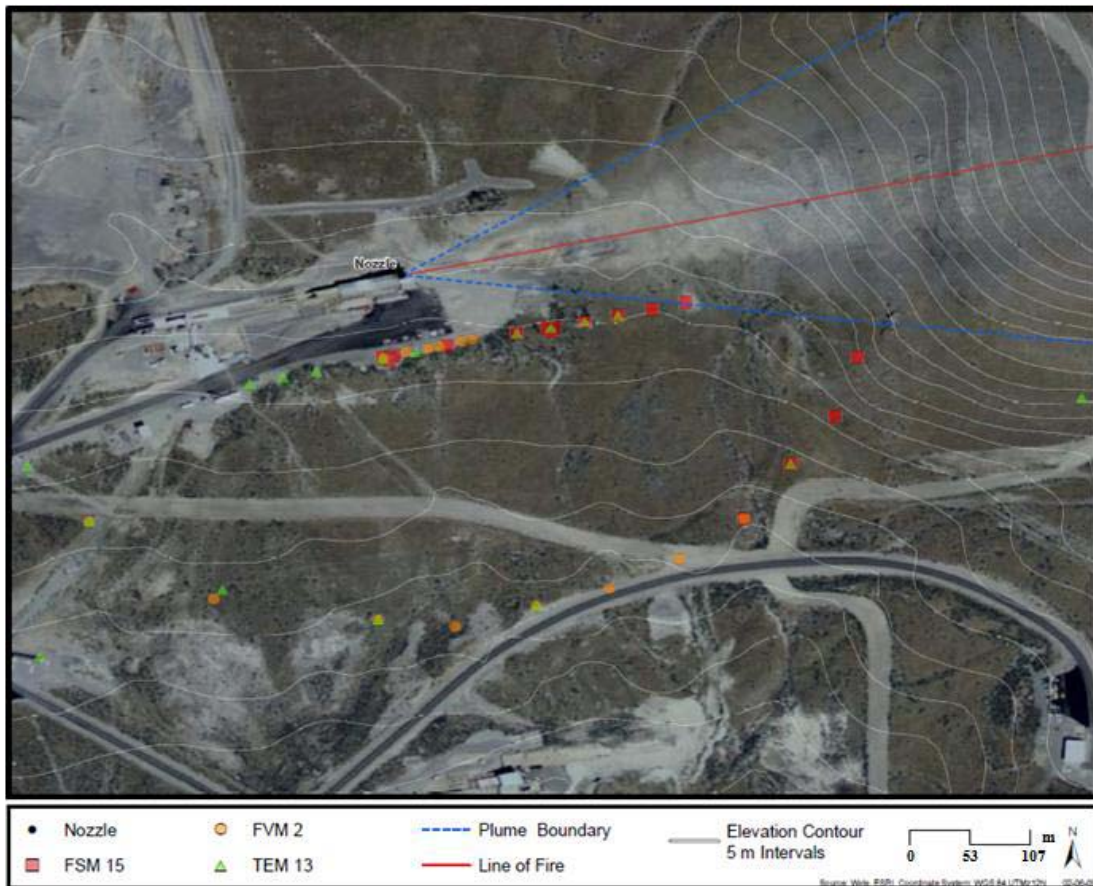

Figure 2. Measurement overview for the three RSRM motor tests at ATK Space Systems.
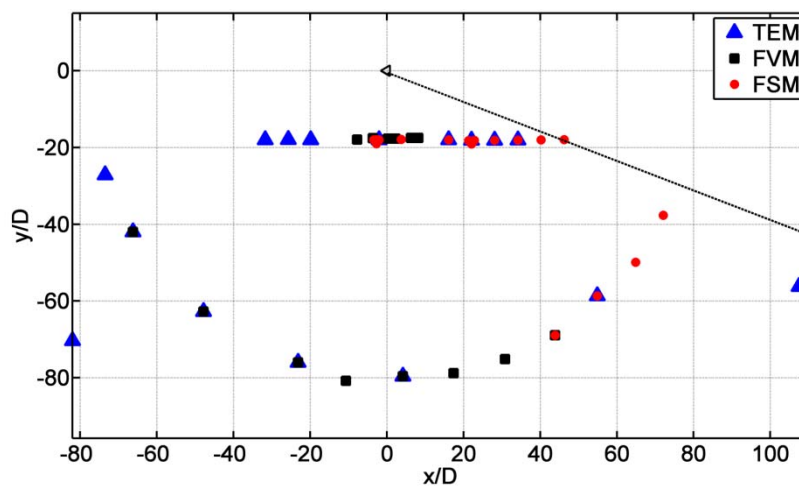

Figure 3. Microphone layout for the three RSRM firings, simplified from Figure 2.

3. Overall Levels

An analysis of the spatial distribution of the overall sound pressure level (OASPL) between 50-60 s during the ~120 s burn has been carried out. The spatial distribution of OASPL is displayed in Figure 4. It is stressed that although the cubic spline interpolation creates a relatively smooth map, the actual variation between the 18D sideline array and 80D arc is unknown. Nor would it be appropriate to assume a simple form of geometric spreading given the uncertain extent of the geometric near field. The color map simply provides a reasonable means to look at the spatial distribution of level simultaneously and to trace the apparent origin of maximum OASPL at the source. In this case, the maximum directivity occurs at ~56° relative to the centerline and the nozzle exit, and the maximum source location appears to be 17-18D at the centerline.
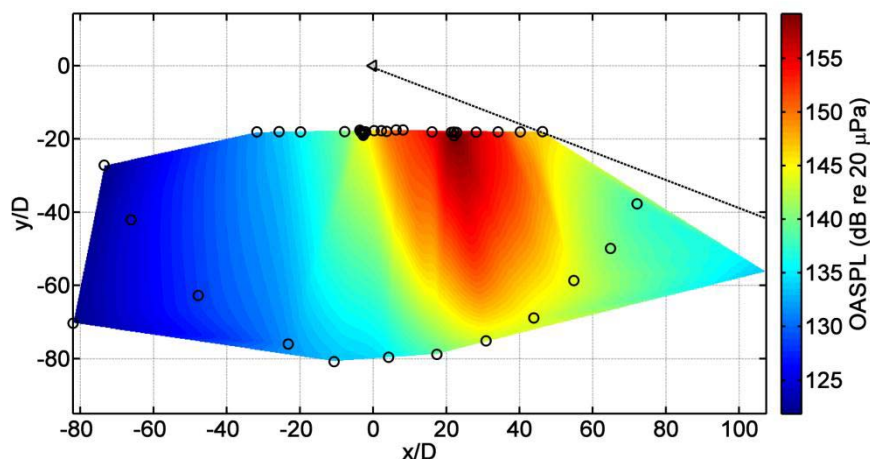

Figure 4. Spatial distribution of overall sound pressure level from the combined motor tests.

Figure 4 uses the averaged OASPL at measurement points common to multiple firings. Figure 5 shows the 18D and 80D arrays separately, revealing the degree of consistency between the measurements. The greatest variation, ±2-3 dB, occurs in the region of maximum OASPL at both arrays, which ranges from 10-35D at 18D and 45-70° at 80D for the 3-dB down point.
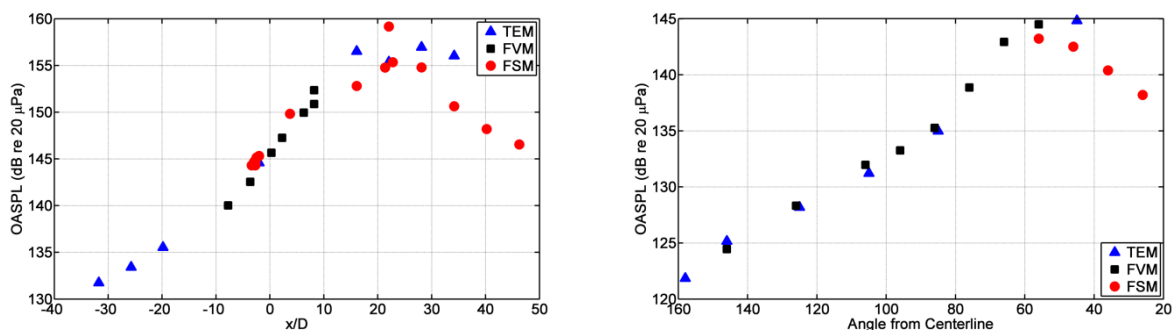

Figure 5. Left: OASPL along the 18D sideline array from each tests. Right: OASPL along the 80D arc.

Figure 4 and Figure 5 show spatial variations for the same 10 s period during the firings. The temporal variation of OASPL during the entire duration of a burn is also of interest. As an example, running OASPL results during TEM-13 at four sideline array locations (x/D = -31, -1, 16, 34) are displayed in Figure 6. Also included is a normalized thrust on a decibel scale and a schematic representation of the horizontal and vertical thrust vectoring. Vertical thrust vectoring occurs at 50-70 s and 90-110 s. It appears that the thrust vectoring has a greater impact on level variation than thrust variation for this firing. The ±1-2 dB oscillations due to horizontal vectoring are visible during the initial part of the test, with the maximum variation occurring far upstream and downstream. The vertical thrust vectoring reveals an increase in level as the plume is elevated above the pad. The change is greatest at the location farthest downstream where the temporal variation in plume direction is greatest, but that does not explain the relatively large change at the x/D= -31 location upstream. Approximately ±1-2 dB oscillations occur at most locations throughout the duration of the firing, with the decrease in thrust mid-firing partially offset by the vertical thrust vectoring. The rapid decay in level at about 110 s tracks the decrease in thrust toward the end of the burn. A similar plot was shown previously by Gee et al.[7] for a smaller solid rocket motor, and the results here could merit further comparison.
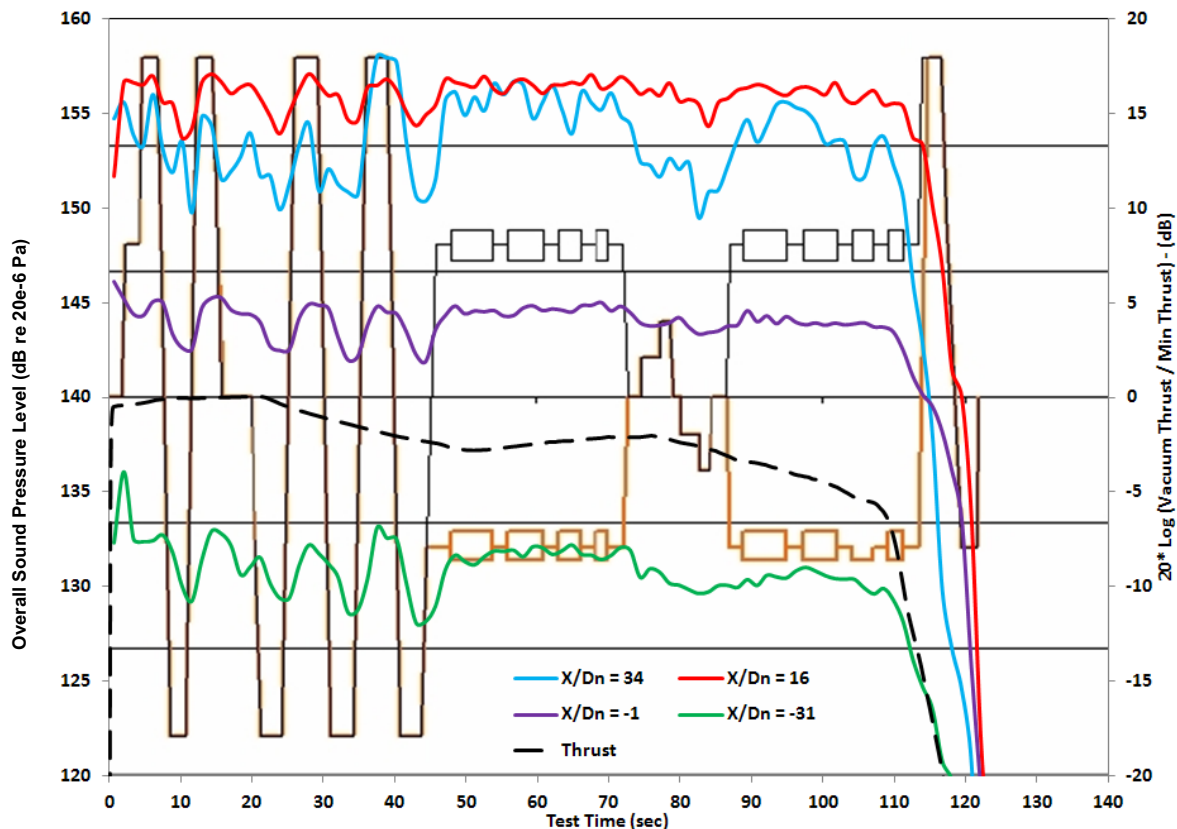

Figure 6. OASPL from the TEM-13 test as a function of time at four sideline locations. Also shown are a normalized thrust profile (dashed line) and schematic representations of the horizontal and vertical thrust vectoring. The vertical thrust vectoring, represented with the boxes, occurs at 50-70 s and 90-110 s.

4. Spectral Analysis

Displayed in Figure 7 are one-third octave band levels for several different frequencies. With increasing frequency, the dominant source location moves upstream, and the directivity shifts toward the sideline. This is characteristic of jet aeroacoustic sources and is included in the launch vehicle loading model.[1] The spatial extent of the source at low frequencies indicates that the 80D arc is likely not in the geometric far field, which could impact the use of these data as directivity indices.[5, 8] However, also apparent is an unnatural "hole" in the downstream data beyond 40D at the 18D array and less than 46° at the 80D arc. It is first readily apparent around 20 Hz, but its prevalence increases as a function of frequency. The cause of this change in the spatial data, which is less noticeable in the OASPL in Figure 4, is explored subsequently, after a discussion of statistical features in the data.
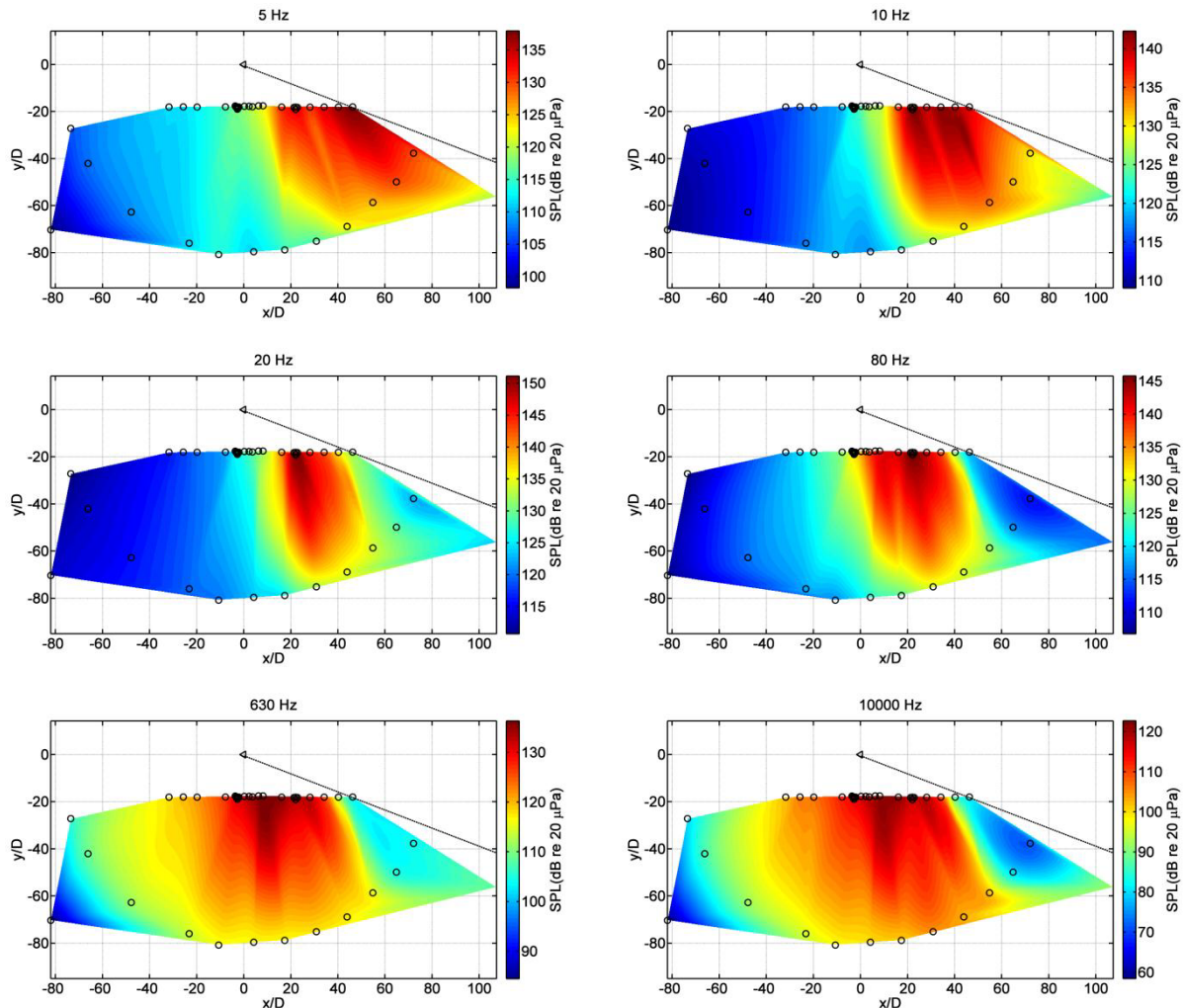

Figure 7. One-third octave band pressure levels from the combined motor tests.

5. Statistical Analysis

In this section, the skewness, or the normalized third central moment of the waveform probability density function, is examined. This is done for both the pressure, $p(t)$, and for its first-order forward time derivative estimate, $\partial p/\partial t$. These measures have been examined for high-amplitude laboratory-scale,[9] full-scale jets,[10, 11,12] and in-flight launch vehicles[13] in the past. Positive waveform skewness, $\text{Sk}\{p(t)\}$, is associated with being a property of high-amplitude jet aeroacoustic sources that peaks around the maximum radiation direction. Less understood are the spatial characteristics of the skewness of the derivative, $\text{Sk}\{\partial p/\partial t\}$, however, recent studies for a nonlinearly propagating sinusoid[14] show that increasing derivative skewness is associated with waveform steepening and the formation of acoustic shocks. The same appears to be true for recent analyses of military[15] and supersonic laboratory-scale jets.[16]

Displayed in Figure 8 is the compiled spatial map of $\text{Sk}\{p(t)\}$, whereas Figure 9 contains both the 18D and 80D values for $\text{Sk}\{p(t)\}$ for the three firings. The maximum skewness values occur in the vicinity of the maximum OASPL (see Figure 4), and there is overall positive skewness, but there is substantial variability both across the measurement aperture and for the different tests at the same locations (see Figure 9). This is particularly true in the downstream, maximum radiation direction. Note the apparent hole in the skewness for the positions farthest aft, noted previously for the high-frequency band pressure levels in Figure 7. However, the overall trend is for positive skewness with maximum values near the peak radiation direction.
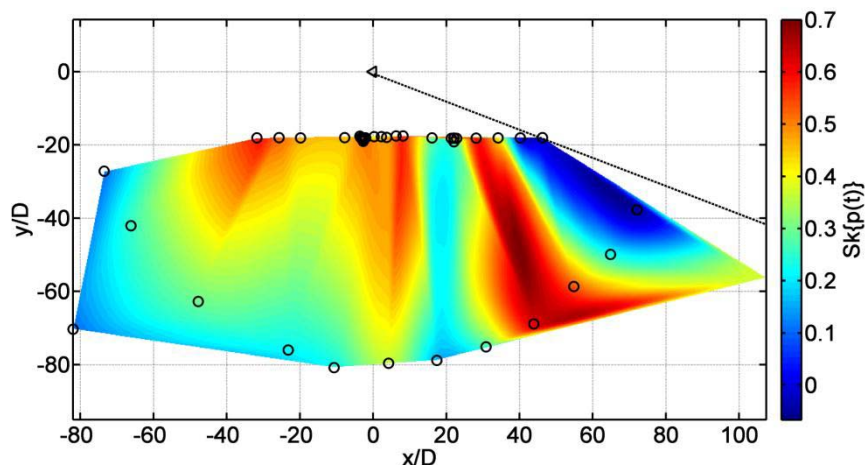

Figure 8. Spatial distribution of waveform skewness from the combined motor tests.
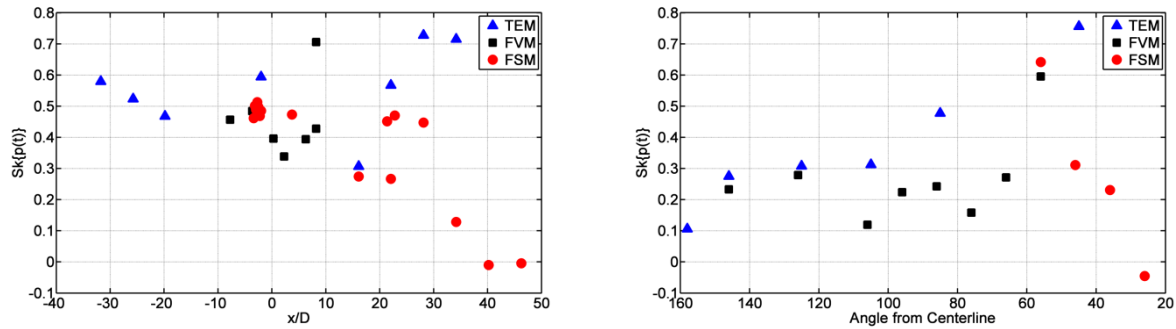
Figure 9. Left: Waveform skewness along the 18D sideline array from each tests. Right: Waveform skewness along the 80D arc.

Figure 10 and Figure 11 show the derivative waveform skewness for the compiled test and for the individual tests along the 18D and 80D arrays. Of significance is the maximum $Sk\{\partial p/\partial t\}$ around the peak radiation direction, the growth of $Sk\{\partial p/\partial t\}$ along virtually all angles, indicating nonlinear wave propagation,[17] and possibly unnatural drop-off at the farthest downstream locations. Figure 11 shows a much greater consistency between the motor tests in the derivative skewness than the waveform skewness. The reason for this is not immediately clear but may suggest environmental conditions could impact near-field evolution of waveform skewness more than acoustic shock formation and derivative skewness. Given that the skewness of a Gaussian process is zero, skewness values in excess of 30 that are increasing indicate a highly non-Gaussian, nonlinear process.
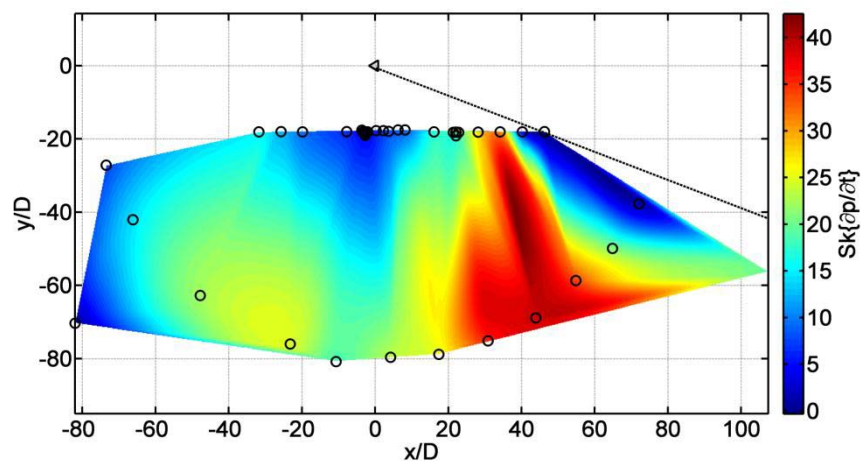

Figure 10. Spatial distribution of the waveform derivative skewness from the combined motor tests.
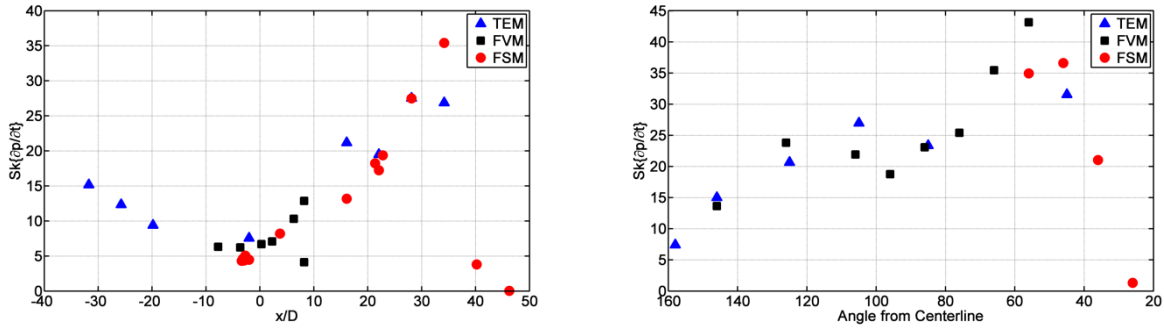
Figure 11. Left: Waveform derivative skewness along the 18D sideline array from each of the tests. Right: Waveform derivative skewenss along the 80D arc.

Figure 12 shows the running Sk$\{\partial p/\partial t\}$ for the TEM-13, similar to the running OASPL plot in Figure 6. Note that the derivative skewness is relatively constant over time at all locations except for the x/D=34 position downstream. At this location, although some of the oscillations in the derivative skewness correspond to the horizontal nozzle movement, the values are significantly larger during the vertical vectoring when the plume is angled upward. This indicates that plume impingement or aeroacoustic scrubbing along the ground can impact the noise generation process such that the shock formation in propagation is affected. This occurs in spite of the fact that the running OASPL in Figure 6 does not appear to change in the same fashion as Sk$\{\partial p/\partial t\}$. The effects of plume impingement are considered in the context of the "hole" in the downstream high-frequency band pressure levels and the skewness.
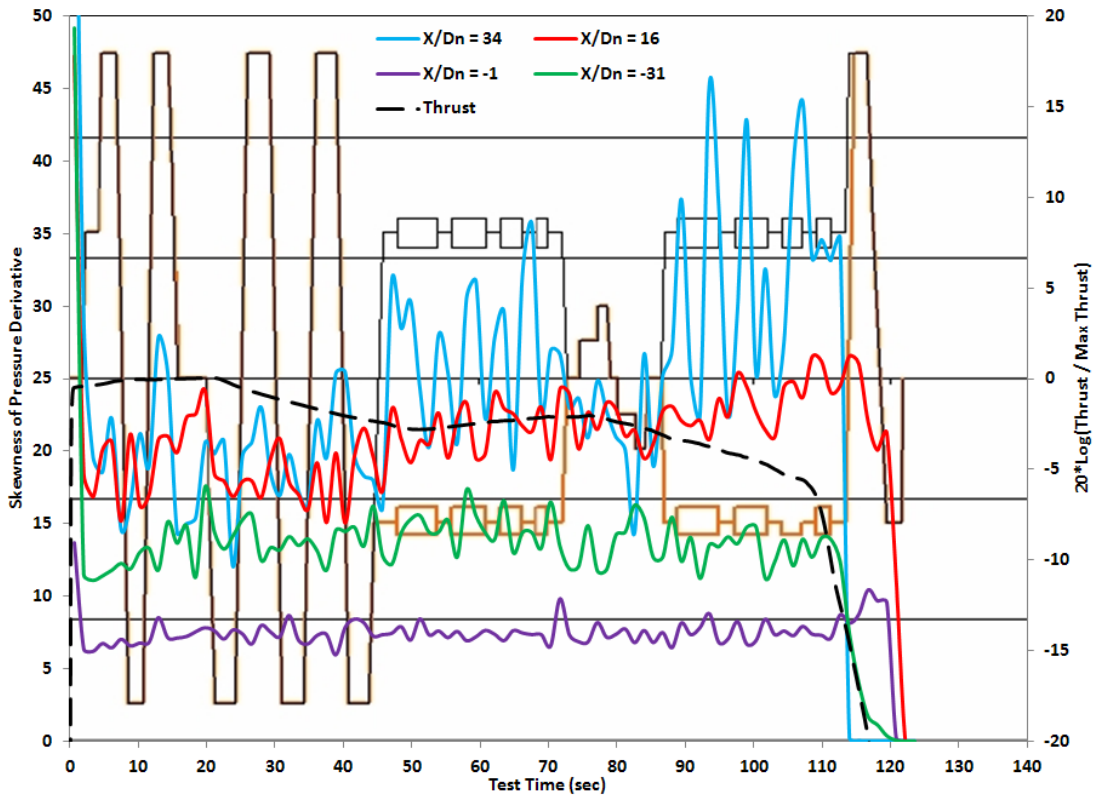

Figure 12. Running waveform derivative skewness during TEM-13 for the same locations as Figure 6.

6. Impact of Plume Impingement

In the previous section, the greater Sk$\{\partial p/\partial t\}$ is related to periods of vertical nozzle vectoring, which reduces plume impingement on the ground. Because Sk$\{\partial p/\partial t\}$ is related to acoustic shocks, and shocks are related to high-frequency spectral content, it was hypothesized that the downstream behavior of the statistics and high-frequency band pressure levels were related to some feature of plume impingement that caused a sudden spatial change in the noise generation process. First, to compare the differences, two channels along the 80D arc were selected for analysis. Channel 28 corresponds to 26° from the FSM-15 test, and channel 31 corresponds to 56°, the maximum radiation angle. The 26° data were part of the downstream "hole" in the spatial maps. Figure 13 shows small waveform segments from the two channels. Note the very different features in the noise waveforms; the data along 26° appears to be random, low-frequency noise whereas the 56° data are shock-like and positively skewed. The power spectral densities (PSDs) between 50-60 s are displayed in Figure 14. Although the shift in peak frequency downward from 56° to 26° is expected, it is the rapid reduction in high-frequency energy above the peak-frequency region and the increased roll-off above 2 kHz for 26° that appears to be most different.

Because the sudden change in spatial behavior appeared at 40D in the sideline measurement array, the terrain was examined for features that could contribute to (1) the reduction in high-frequency energy and (2) the "randomization" of the noise generation process that could result in radically reduced waveform and derivative skewness. It is very apparent from Figure 15 that 40D corresponds to the end of the "bowl" carved out of the hillside over the many years of firings that occurred at that test stand. Therefore, it is very likely that 40D corresponds to significantly greater plume impingement. This could possibly lead to a breakdown of the large turbulent structures associated with Mach wave radiation, leaving a more random, spatially incoherent noise generation process. This would help to explain the dramatically different waveform shapes in Figure 13.
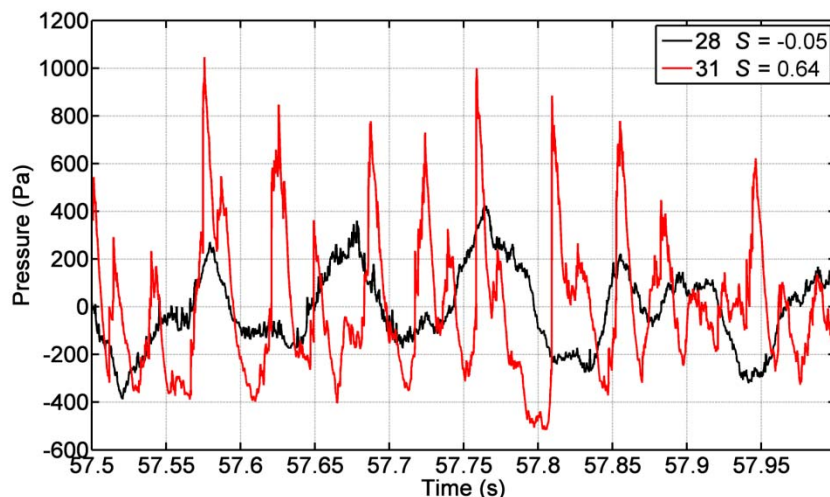

Figure 13. Waveform segments from FSM-15 at 26° (channel 28) and 56° (channel 31). Shown in the legend are the waveform skewness values.
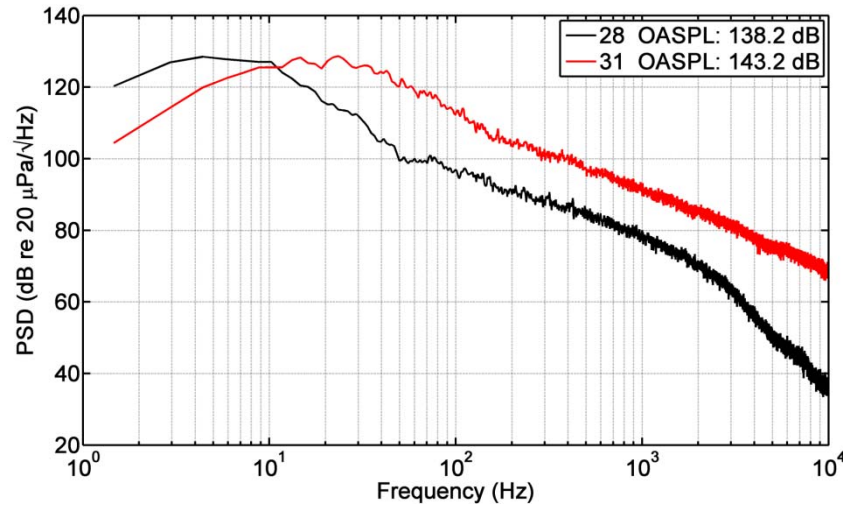
Figure 14. Power spectral densities from FSM-15 at 26° (channel 28) and 56° (channel 31) between 50-60 s. The corresponding OASPL is shown in the legend.
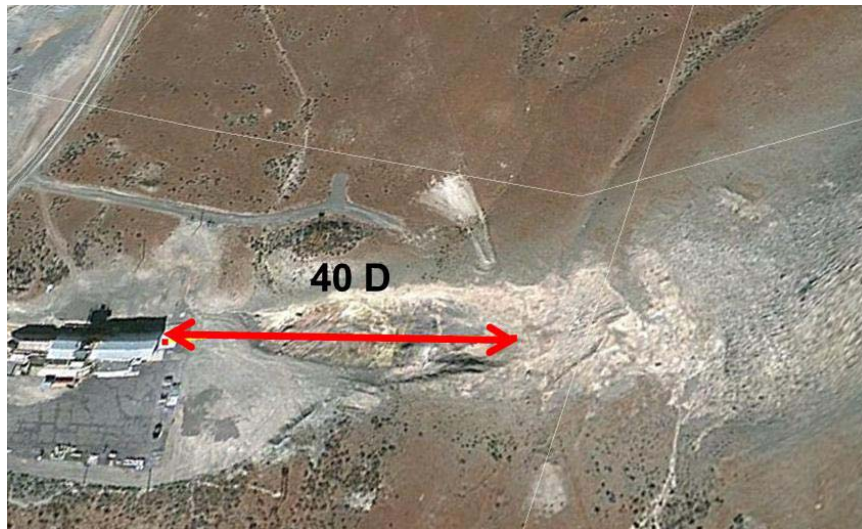

Figure 15. Zoomed-in satellite view of the topography from Google Earth, annotated with the ~40D extent.

7. Conclusion

This paper has provided additional spectral and statistical analyses of reusable solid rocket motor (RSRM) firings. These can be used in the future to compare against data from other launch vehicles[7,18] and other high-amplitude jet sources. The anomalous behavior of the high-frequency bands and the skewness far downstream is likely caused by plume impingement on the hillside. These results have implications for further study of vertical launch or static test scenarios, where far greater plume impingement will likely have a larger impact on the noise generation process and the acoustic loading on the launch pad, vehicle, and payloads.

References

[1] K.M. Eldred, "Acoustic loads generated by the propulsion system," NASA SP-8072, (1971).

[2] R. J. Kenny, C. Hobbs, K. Plotkin, and D. Pilkey, "Measurement and characterization of Space Shuttle solid rocket motor plume acoustics," AIAA paper 2009-3161, May 2009.

[3] J. Haynes and R. Kenny, "Modifications to the NASA SP-8072 Distributed Source Method II for Ares I lift-off environment predictions", AIAA paper 2009-3160, May 2009.

[4] K. J. Plotkin and B. T. Vu, "Further development of a launch pad noise prediction model," J. Acoust. Soc. Am. **130**, 2510 (2011).

[5] M. M. James, A. R. Salton, and K. L. Gee, "Full-scale rocket motor acoustic tests and comparisons with models: Revisiting the empirical curves," J. Acoust. Soc. Am. **132**, 1991 (2012).

[6] M. M. James, A. R. Salton, and K. L. Gee, "Full-scale rocket motor acoustic tests and comparisons with models: Updates and comparisons with SP-8072," J. Acoust. Soc. Am. **132**, 1991 (2012).

[7] K. L. Gee, J. H. Giraud, J. D. Blotter, and S. D. Sommerfeldt, "Energy-based acoustical measurements of rocket noise," AIAA paper 2009-3165, May 2009.

[8] J. H. Giraud and K. L. Gee, "Directivity indices for rocket noise modeling: Measurement considerations," J. Acoust. Soc. Am. 127, 1772 (2010).

[9] B. P. Petitjean, K. Viswanathan, and D. K. McLaughlin, "Acoustic pressure waveforms measured in high speed jet noise experiencing nonlinear propagation," Int. J. Aeroacoust. **5**, 193-215 (2006).

[10] J. E. Ffowcs Williams, J. Simson, and V. J. Virchis, "'Crackle': An annoying component of jet noise," J. Fluid Mech. 71, 251-271 (1975).

[11] K. L. Gee, V. W. Sparrow, A. A. Atchley, and T. B. Gabrielson, "On the perception of crackle in high-amplitude jet noise," AIAA J. **45**, 593-598 (2007).

[12] S. A. McInerny, K. L. Gee, J. M. Downing, and M. M. James, "Acoustical nonlinearities in aircraft flyover data," AIAA paper 2007-3654, May 2007.

[13] S. A. McInerny, "Launch vehicle acoustics Part 2: Statistics of the time domain data," J. Aircraft **33**, 518-523 (1996).

[14] M. R. Shepherd, K. L. Gee, and A. D. Hanford, "Evolution of statistics for a nonlinearly propagating sinusoid," J. Acoust. Soc. Am. **130**, EL8-EL13 (2011).

[15] K. L. Gee, J. Micah Downing, M. M. James, R. L. McKinley, R. C. McKinley, T. B. Neilsen, and A. T. Wall, "Near-field shock formation in noise propagation from a high-power jet aircraft," J. Acoust. Soc. Am. **133**, EL88-EL93 (2013).

[16] K. L. Gee, T. B. Neilsen, and A. A. Atchley, "Near-field skewness in laboratory-scale supersonic jet data," submitted to J. Acoust. Soc. Am. (2012).

[17] M. B. Muhlestein, K. L. Gee, D. C. Thomas, and T. B. Neilsen, "Prediction of nonlinear propagation of noise from a solid rocket motor," J. Acoust. Soc. Am. **132**, 1992 (2012).

[18] M. M. James and K. L. Gee, "Advanced acoustic measurement system for rocket noise source characterization," Proc. Internoise 2012, paper in12_1127 (2012).